https://doi.org/10.5194/essd-2026-447
Preprint. Discussion started: 12 August 2026

Open Access Earth System Science Data Discussions

A 1 km resolution dataset of Northern Hemisphere permafrost active layer thickness (2000–2024)

Yujiao Wei[1], Zhaoqi Wu[1], Jiaxue Wang[1], Huanfeng Shen[1], Yiyun Chen[1, 2, 3]

[1] School of Resource and Environmental Sciences, Wuhan University, Wuhan 430079, China
[2] Key Laboratory of Digital Cartography and Land Information Application Engineering, Ministry of Natural Resources, Wuhan 430079, China
[3] Hubei Luojia Laboratory, Wuhan University, Wuhan 430079, China

Correspondence to: Yiyun Chen (chenyy@whu.edu.cn)

Abstract. Active layer thickness (ALT) is a key indicator of permafrost change, with important implications for soil hydrothermal conditions, carbon feedbacks, ecosystem processes, and cold-region infrastructure. However, hemispheric-scale ALT mapping remains challenging because field observations are sparse and unevenly distributed, while thaw depth is controlled by complex and nonlinear environmental interactions. Here, we compiled 2,196 annual ALT observations and developed an ensemble spatiotemporal machine-learning framework to reconstruct a continuous annual ALT dataset at 1 km resolution for the Northern Hemisphere permafrost region from 2000 to 2024. Spatial leave-one-site-out cross-validation yielded an ensemble R^2 of 0.76 and an RMSE of 60.48 cm. Independent temporal evaluation showed a significant correlation between observed and predicted Sen's slopes (r = 0.73, p < 0.001), with 86.8% agreement in trend direction. The dataset reproduced broad latitudinal and elevational patterns, biome-related differences, and interannual variability. Comparisons with two existing 1 km hemispheric products showed that our reconstruction occupied an intermediate position in hemispheric mean ALT while preserving relatively fine spatial variability. Substantial inter-product differences in both magnitude and spatial structure further highlighted persistent structural uncertainty in large-scale ALT mapping. Pixel-wise uncertainty maps further provide spatially explicit information on prediction confidence. This dataset provides a spatially detailed, temporally continuous, and uncertainty-explicit resource for regional- to hemispheric-scale studies of permafrost dynamics, carbon-cycle feedbacks, ecosystem and hydrological responses, and infrastructure exposure.

1 Introduction

Permafrost covers approximately 21% of the land area in the Northern Hemisphere, constituting a vital component of the global cryosphere (Obu et al., 2019). As the key surface interface for energy and moisture exchange between permafrost and the atmosphere, the active layer is highly sensitive to climate change (Cheng et al., 2019; McGuire et al., 2009). Over the past few decades, as arctic amplification has intensified, a general thickening of the active layer has become a widely recognized trend (Hu et al., 2021; IPCC, 2021; Mu et al., 2023). This change not only profoundly impacts hydrological (Tananaev and Lotsari, 2022) and ecological processes (Li et al., 2026) in cold regions but also promotes the decomposition and release of

https://doi.org/10.5194/essd-2026-447
Preprint. Discussion started: 12 August 2026

Open Access Earth System Science Data Discussions

deep-seated, ancient organic carbon, creating a positive feedback loop that intensifies global warming (Gasser et al., 2018; Koven et al., 2011; Schuur et al., 2015). Simultaneously, it threatens the thermal stability and structural integrity of infrastructure in cold regions (Hjort et al., 2018; Nelson et al., 2001). Therefore, generating a high-resolution, temporally continuous, and spatially explicit dataset of active layer thickness (ALT) across the Northern Hemisphere is urgently needed to support Earth system modeling, carbon budget estimations, and infrastructure risk assessments.

However, reconstructing large-scale, long-term dynamic datasets of ALT remains challenging. Traditional in situ observation networks are sparsely and unevenly distributed, failing to adequately capture the spatial heterogeneity of vast permafrost regions (Ding et al., 2025; Shen et al., 2023). In recent years, with the advancement of Earth observation big data and remote sensing, machine learning algorithms have demonstrated tremendous potential in addressing complex surface environmental issues due to their powerful nonlinear fitting capabilities (Aalto et al., 2018; Chadburn et al., 2017; Ran et al., 2022; Xu et al., 2017). However, existing studies predominantly employ static spatial modeling strategies (Ni et al., 2021; Ran et al., 2022; Wang et al., 2019), which utilize multi-year average climate states to predict the spatial distribution of ALT, neglecting the critical temporal dynamics driven by interannual climate fluctuations. Meanwhile, constrained by the scale of observational samples, models often exhibit overfitting risks (Vabalas et al., 2019).

Recently, a few 1 km hemispheric-scale ALT datasets have been developed to capture permafrost dynamics over time. For instance, Westermann et al. (2024) produced a physics-based ALT time series for 1997–2021, whereas Peng et al. (2024) developed a machine-learning-based dataset extending from 1850 to 2100. Such differences likely arise from contrasting model structures, environmental predictors, parameterizations, and permafrost masks, and make it difficult for users to identify robust regional signals (Liu et al., 2023; Peng et al., 2024; Westermann et al., 2024). In particular, existing machine-learning products may capture broad climatic gradients but show relatively smooth spatial patterns or locally abrupt transitions, limiting their representation of the strong environmental heterogeneity characteristic of permafrost landscapes. Moreover, these existing high-resolution products rarely provide robust, spatially explicit uncertainty estimations. Therefore, there is still a need for an independently reconstructed ALT dataset that more explicitly evaluates spatial generalization, temporal reliability, local spatial heterogeneity, and prediction uncertainty.

To address these limitations, this study aims to reconstruct a continuous annual ALT dataset at 1 km spatial resolution for the Northern Hemisphere permafrost region from 2000 to 2024. After quality control and spatiotemporal matching, 2,196 annual ALT observations from 201 monitoring sites were used for model development. Five machine-learning algorithms, Random Forest, Gradient Boosting Decision Tree, eXtreme Gradient Boosting, CatBoost, and LightGBM, were systematically evaluated using leave-one-site-out cross-validation, ensuring that predictions were assessed at sites entirely excluded from model training. The best-performing algorithms were then combined to generate the final ensemble product. Temporal reliability was further assessed using site-level out-of-fold prediction series, while repeated site-based resampling was used to quantify pixel-wise prediction uncertainty. The resulting dataset was designed to preserve regional ALT gradients and spatial heterogeneity while providing explicit information on spatial accuracy, temporal performance, and prediction uncertainty.

https://doi.org/10.5194/essd-2026-447
Preprint. Discussion started: 12 August 2026

2 Materials and methods

2.1 Study area

The study area encompasses the extensive permafrost domain of the Northern Hemisphere, a critical component of the global climate system (Fig. 1a). It spans the high-latitude Pan-Arctic belt, including Siberia, Alaska, and the Canadian Arctic Archipelago, as well as high-altitude mid-latitude regions like the Tibetan Plateau and the Mongolian Plateau. The permafrost distribution exhibits significant spatial heterogeneity, with a clear gradient from continuous permafrost in the high-latitude interior to discontinuous, sporadic, and isolated zones in the south (Obu et al., 2019) (Fig. 1b). The continuous zone is characterized by high thermal stability, whereas the fragmented marginal zones are more sensitive to temperature fluctuations. Ecologically, the land surface is characterized by distinct biomes reflecting hydrothermal gradients (Fig. 1c). The high Arctic is predominantly covered by Tundra, which transitions southward into extensive Boreal Forests (Taiga) that act as a thermal buffer over the permafrost. High-altitude regions like the Tibetan Plateau are dominated by Montane Grasslands and Shrublands (Olson et al., 2001). This complex combination of geomorphology, permafrost zonation, and vegetation creates a highly heterogeneous background for ALT evolution.

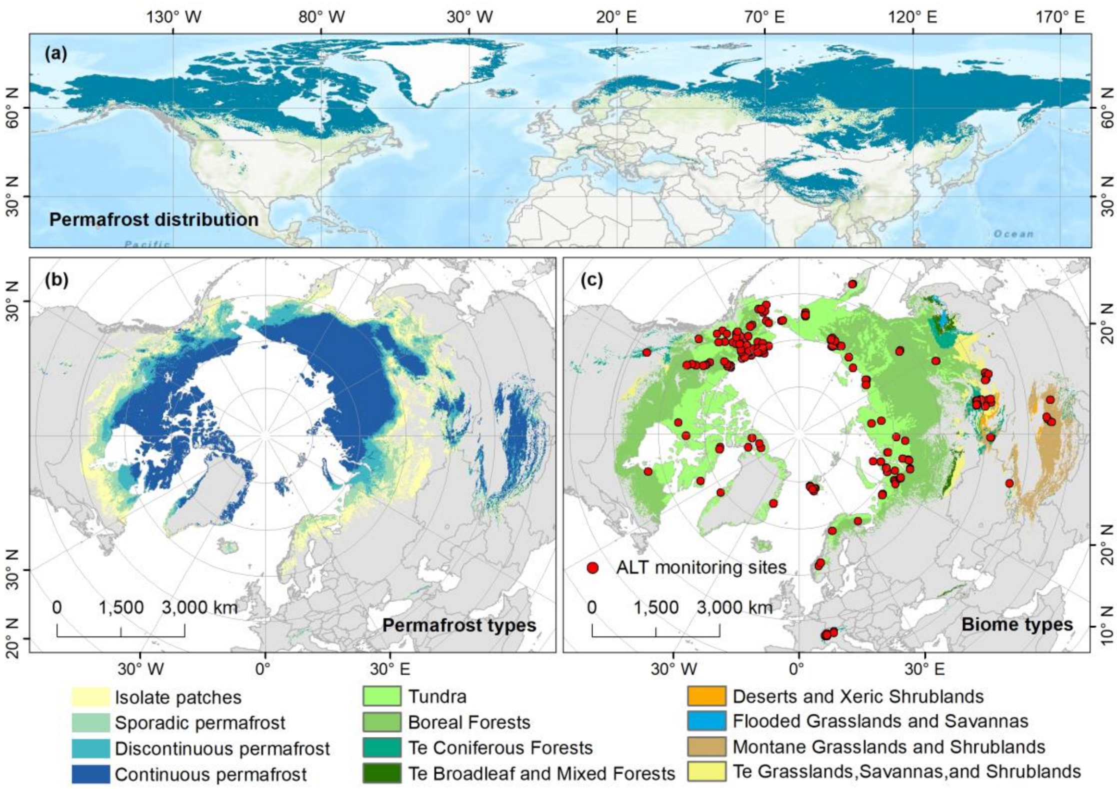

Figure 1. Distribution range of permafrost regions in the Northern Hemisphere (a), distribution of permafrost types (b), biome types and ALT sites (c). Te, Temperate.

https://doi.org/10.5194/essd-2026-447
Preprint. Discussion started: 12 August 2026

2.2 Permafrost distribution data

The permafrost distribution used in this study was obtained from the 1 km Northern Hemisphere permafrost dataset developed by Obu et al. (2019), which represents near-surface permafrost conditions for 2000–2016. The continuous, discontinuous, sporadic, and isolated-patch permafrost classes were combined to define the spatial domain of the reconstruction. This permafrost extent was applied as a fixed mask to all annual ALT maps from 2000 to 2024; therefore, the dataset represents temporal changes in ALT within the mapped permafrost domain rather than changes in permafrost extent itself. The dataset is publicly accessible via PANGAEA (Obu et al., 2018).

2.3 ALT observations

ALT observations were compiled to establish an observation-based reference dataset for model development and evaluation across the Northern Hemisphere permafrost region. The primary data sources were the Circumpolar Active Layer Monitoring (CALM) program and the Global Terrestrial Network for Permafrost (GTN-P), which provide long-term ALT observations from the Pan-Arctic and high-elevation permafrost regions.

The compiled ALT records were obtained using several established monitoring techniques. At sites with relatively shallow active layers, ALT was commonly measured by mechanical probing near the end of the thawing season. At sites where the thaw depth exceeded the practical range of probing, ALT was determined from borehole ground-temperature profiles by identifying or interpolating the depth of the 0 °C isotherm, or was monitored using thaw tubes (Peng et al., 2023). These methods collectively provide observations of the maximum seasonal thaw depth, although differences among measurement techniques may introduce additional observational uncertainty.

The monitoring sites span broad latitudinal, longitudinal, elevational, and environmental gradients across the Northern Hemisphere permafrost region (Fig. 1). However, their spatial distribution is uneven, reflecting the availability of established monitoring networks. Monitoring sites are relatively concentrated in regions such as Alaska, northern Canada, and northern Europe, whereas parts of interior Siberia and the Tibetan Plateau remain comparatively underrepresented. A quality-control procedure was applied to the compiled observations before model development. Records with missing or implausible coordinates, incomplete site metadata, duplicated entries, or unresolved inconsistencies in site location, observation year, or ALT value were removed.

2.4 Environmental variables

To reconstruct annual ALT across the Northern Hemisphere, we compiled a multi-source environmental predictor dataset consisting of 17 environmental variables, including nine time-varying drivers and eight time-invariant environmental controls. The predictor set was designed to represent the climatic, vegetation, topographic, soil, and ecosystem conditions influencing ALT variability. To ensure spatial consistency among datasets, all raster layers were reprojected to a common coordinate reference system, clipped to the Northern Hemisphere permafrost extent, and resampled to a unified spatial resolution of 1 km

https://doi.org/10.5194/essd-2026-447
Preprint. Discussion started: 12 August 2026

before model development. Detailed information on all environmental variables, including their data sources, spatial and temporal resolutions, temporal coverage, and references, is provided in Table S1.

Prior to model development, the initial predictor set was screened to reduce redundancy and potential multicollinearity. Variables showing negligible correlations with ALT were first excluded, after which Pearson correlation analysis was conducted among the remaining continuous predictors to identify highly correlated variables. The detailed screening results and the final predictor set are presented in Section 3.1.

2.4.1 Time-varying drivers

Dynamic predictors were used to characterize the interannual variability of climate and vegetation associated with ALT dynamics. Climate-related variables included mean annual temperature (MAT), annual maximum temperature (MATmax), annual minimum temperature (MATmin), mean annual precipitation (MAP), thawing index (TI), freezing index (FI), solar radiation (SR), and snow depth (SDE).

Monthly average maximum temperature (tmax), monthly average minimum temperature (tmin), and total monthly precipitation for 2000–2024 were obtained from the WorldClim historical monthly weather dataset, which provides downscaled monthly climate data based on WorldClim v2.1. Monthly mean air temperature was calculated as the average of monthly tmax and tmin. MAT was subsequently calculated as the average of the 12 monthly mean temperatures, whereas MAP was calculated as the sum of monthly precipitation. MATmax and MATmin were defined as the maximum and minimum monthly mean temperatures within each year, respectively. The TI and FI were derived from monthly mean air temperature by weighting each monthly value by the number of days in the corresponding month. Specifically,

$$TI = \sum_{i=1}^{12} max(T_i, 0) \times D_i \tag{1}$$

$$FI = \sum_{i=1}^{12} |min(T_i, 0)| \times D_i \tag{2}$$

where T_i is the monthly mean air temperature of month i, and D_i is the corresponding number of days in that month. TI and FI represent the annual cumulative positive and negative degree-days, respectively.

Monthly SR and SDE were obtained from the ERA5-Land reanalysis dataset. Annual SR was calculated as the mean of the 12 monthly values, whereas winter SDE was calculated as the average snow depth from October of the previous year through April of the current year, representing snow conditions during the cold season that predominantly influence subsequent active layer development. Vegetation dynamics were represented by the annual maximum normalized difference vegetation index (NDVI), obtained from the Global 1 km Resolution Annual Maximum Composite NDVI Dataset (V3) (Wang et al., 2026). For each ALT observation, the corresponding annual values of all dynamic predictors were extracted according to the observation year to ensure temporal consistency between predictor variables and ALT measurements.

https://doi.org/10.5194/essd-2026-447
Preprint. Discussion started: 12 August 2026

2.4.2 Time-invariant environmental controls

Static predictors were used to characterize the spatial heterogeneity of terrain, soil, and ecosystem conditions. Topographic variables included elevation (Elev) and slope (Slope). Elevation was obtained from the General Bathymetric Chart of the Oceans (GEBCO) global elevation dataset, and slope was subsequently derived from the elevation using standard terrain analysis procedures. Soil properties were obtained from the SoilGrids database and included bulk density (BD), coarse fragment content (CF), sand content (Sand), silt content (Silt), and clay content (Clay). To better represent ecological differences across the Northern Hemisphere permafrost region, biome type (Biome) was additionally incorporated as a categorical predictor describing the dominant vegetation community and ecosystem type (Olson et al., 2001).

2.5 Spatiotemporal reconstruction of ALT

2.5.1 Construction of the modelling dataset

A spatiotemporal feature-matching strategy was used to construct the modelling dataset. For each ALT observation, annual dynamic environmental covariates were extracted for the corresponding observation year, while static topographic and soil properties were assigned according to the station location. Some records were located near water bodies, outside the valid coverage of individual remote-sensing products, or in areas with missing soil or vegetation information. Records containing missing values in any retained predictor were therefore excluded to ensure a complete and internally consistent modelling dataset. After data matching, quality control, and predictor screening, 2,196 annual ALT records from 201 monitoring sites during 2000–2020 were retained for model development and evaluation.

2.5.2 Model development and spatial validation

Five machine-learning algorithms were initially evaluated as candidate models: Random Forest (RF), Gradient Boosting Decision Tree (GBDT), eXtreme Gradient Boosting (XGBoost), Categorical Boosting (CatBoost), and Light Gradient Boosting Machine (LightGBM). Model transferability to previously unseen locations was assessed using leave-one-site-out cross-validation (LOSO-CV). In each fold, all annual observations from one monitoring site were withheld simultaneously, and the model was trained using observations from all remaining sites. The fitted model was then used to predict ALT for every available year at the withheld site. This procedure ensured that no observations from the evaluated site were included in the corresponding model fitting and avoided information leakage among repeated annual measurements from the same location. The spatially independent out-of-fold predictions obtained from all LOSO folds were pooled to evaluate model performance. Predictive performance was assessed using the coefficient of determination (R^2), Pearson correlation coefficient (r), root mean square error (RMSE), mean absolute error (MAE), and concordance correlation coefficient (CCC). These metrics respectively describe explained variation, linear correspondence, overall prediction error, average absolute deviation, and agreement between observed and predicted ALT (Wei et al., 2026). Based on their overall LOSO performance and complementary

https://doi.org/10.5194/essd-2026-447
Preprint. Discussion started: 12 August 2026

predictive behaviour, CatBoost and LightGBM were selected for final ensemble construction. For each observation or grid cell, the ensemble prediction was calculated as the arithmetic mean of the two model predictions.

2.5.3 Dataset production

After the predictor set, model configurations, and ensemble rule had been fixed through LOSO-CV, CatBoost and LightGBM were refitted using all available records. The two full-data models were then applied to the annual environmental covariates to generate Northern Hemisphere annual maximum ALT maps for 2000–2024. The final ALT estimate for each grid cell and year was obtained by averaging the corresponding CatBoost and LightGBM predictions. Most field observations used for model development were collected during 2000–2020. Consequently, the maps for 2021–2024 represent temporal extrapolations based on relationships learned from the historical observation period. These predictions assume that the relationships between ALT and the selected climatic, vegetation, topographic, and soil covariates remain sufficiently stable when transferred to the subsequent years (Blois et al., 2013).

2.5.4 Temporal validation

To evaluate the temporal reliability of the reconstructed ALT dataset, temporal validation was performed using the site-level out-of-fold predictions generated by LOSO-CV. Validation based solely on a limited number of representative monitoring sites may be strongly influenced by site-specific environmental conditions and therefore may not provide a comprehensive assessment for a hemispheric-scale product. Accordingly, all eligible long-term monitoring sites were included in the temporal evaluation.

In each LOSO iteration, all annual ALT observations from one monitoring site were excluded from model training, and the ALT time series for that site was predicted using models trained with observations from all remaining sites. Consequently, the predicted ALT series for each validation site was generated without using any observations from that site during model training, allowing temporal performance to be evaluated at a spatially withheld location. To ensure reliable estimation of long-term trends and interannual variability, only monitoring sites with at least 10 years of ALT observations during 2000–2020 were included. This resulted in a total of 68 monitoring sites for temporal validation.

For each validation site, the LOSO-derived annual ALT predictions were compared with the corresponding observations. Long-term temporal performance was evaluated by comparing the Sen's slopes of the observed and predicted ALT time series. Trend agreement was quantified using the Pearson correlation coefficient between observed and predicted Sen's slopes, the proportion of sites with consistent trend directions, and the mean absolute slope error (MASE), calculated as:

$$MASE = \frac{1}{n}\sum_{i=1}^{n}\left|\beta_{pred,i} - \beta_{obs,i}\right| \tag{3}$$

where $\beta_{pred,i}$ and $\beta_{obs,i}$ denote the Sen's trend slopes of the predicted and observed ALT time series at the i-th monitoring site, respectively, and n is the number of validation sites.

https://doi.org/10.5194/essd-2026-447
Preprint. Discussion started: 12 August 2026

The ability of the model to reproduce the amplitude of interannual ALT fluctuations was evaluated using the fluctuation amplitude ratio (FAR), defined as:

$$FAR = \frac{\sigma_{pred,detrended}}{\sigma_{obs,detrended}} \tag{4}$$

Where $\sigma_{pred,detrended}$ and $\sigma_{obs,detrended}$ are the standard deviations of the detrended predicted and observed ALT time series, respectively. Detrending was performed by removing the linear trend from each time series prior to calculating the standard deviation, thereby isolating interannual variability from long-term change. A FAR close to 1 indicates that the reconstructed ALT series reproduces the observed fluctuation amplitude well, whereas values below or above 1 indicate underestimation or overestimation of temporal fluctuations, respectively. The overall performance was summarized using the median FAR across the 68 validation sites.

In addition to these quantitative evaluations, time-series comparisons were presented for six representative long-term monitoring sites to provide a direct visualization of site-level temporal performance. For each site, observed ALT was compared with both the LOSO-CV prediction and the prediction extracted from the final model trained using all available observations. The LOSO-CV series illustrates model performance when the site is entirely excluded from training, whereas the final-model series represents the corresponding values in the released ALT dataset.

2.6 Uncertainty quantification

Prediction uncertainty was quantified independently of the LOSO evaluation using repeated site-level subsampling. After the predictor set, model configurations, and ensemble rule had been fixed, 80% of the monitoring sites were randomly selected without replacement in each realization, with all annual observations from the selected sites retained together. This procedure was repeated 100 times to generate 100 site-resampled training datasets.

For each realization, CatBoost and LightGBM were refitted separately using the corresponding subsampled dataset and applied to the annual environmental covariates. The predictions from the two models were averaged to obtain one ensemble ALT realization for each grid cell and year. For each grid cell, the 2.5th and 97.5th percentiles of the 100 ensemble predictions were taken as the lower and upper bounds of the empirical 95% prediction interval (Wei et al., 2025).

Relative uncertainty was calculated by normalizing the width of the empirical prediction interval by the mean ensemble prediction:

$$RU = \frac{Q_{97.5} - Q_{2.5}}{ALT_{mean}} \times 100\% \tag{5}$$

where RU is the relative uncertainty; $Q_{97.5}$ and $Q_{2.5}$ are the 97.5th and 2.5th percentiles of the 100 site-resampled ensemble predictions, respectively, and ALT_{mean} is their mean. Lower RU values indicate that the predicted ALT is less sensitive to variation in the spatial composition of the training-site network, whereas higher values indicate greater variation among the site-resampled model realizations.

https://doi.org/10.5194/essd-2026-447
Preprint. Discussion started: 12 August 2026

2.7 Statistical analysis of the ALT dataset

Statistical analyses were conducted to characterize the spatial and temporal patterns of the reconstructed ALT dataset. Annual mean ALT across the Northern Hemisphere permafrost domain was calculated for each year from 2000 to 2024. To examine long-term changes in ALT structure, continuous ALT values were classified into predefined depth intervals, and the proportional area of each class was calculated for six selected years. Latitudinal and elevational gradients were analysed by grouping valid permafrost pixels into 5° latitude intervals and elevation bins. To reduce geographic heterogeneity, elevational analyses were performed separately for high-latitude (>60°N, elevation <2.0 km) and high-elevation regions (25–45°N, elevation >3.5 km).

The reconstructed ALT dataset was further overlaid with the Northern Hemisphere permafrost zonation map and the global biome dataset. Mean ALT and the distribution of pixel-level ALT values were calculated for each permafrost zone and biome type using all valid overlapping pixels. Differences among categories were visualized using violin plots with embedded boxplots.

3 Results and discussion

3.1 Selection of environmental variables

Pearson correlation analysis was used to examine the bivariate associations between ALT and the continuous environmental predictors and to identify potential redundancy among predictors (Fig. 2). ALT exhibited a strong correlation with Elev (r = 0.67), indicating that topography strongly influences active layer distribution at the macro-scale. Thermal and radiation factors followed, with MAT, FI, and SR exhibiting correlation coefficients of 0.60, –0.58, and 0.57, respectively, indicating broad associations between ALT and regional thermal and energy conditions. Additionally, MAP and CF also showed strong correlations with ALT (both 0.50).

Additionally, the correlation coefficient matrix served as a critical feature selection step prior to modeling in this study, aiming to eliminate multicollinearity and enhance model efficiency by removing redundant variables. Clay was excluded because its correlation with ALT was negligible (r = 0.03). MATmax was removed because it was strongly correlated with TI (r = 0.92), whereas MATmin was excluded because it was highly correlated with MAT (r = 0.76) and MAP (r = 0.75). FI was also removed because of its strong collinearity with MAT (r = −0.95) and MATmin (r = −0.90). In addition, Sand and Silt were strongly negatively correlated (r = −0.90); therefore, only Silt was retained to represent soil texture and reduce feature redundancy. Following this screening process, 12 environmental variables were ultimately retained as input features for subsequent spatiotemporal modeling: SR, MAT, MAP, SDE, TI, NDVI, Biome, Elev, Slope, BD, CF, and Silt.

https://doi.org/10.5194/essd-2026-447
Preprint. Discussion started: 12 August 2026

Open Access Earth System Science Data Discussions

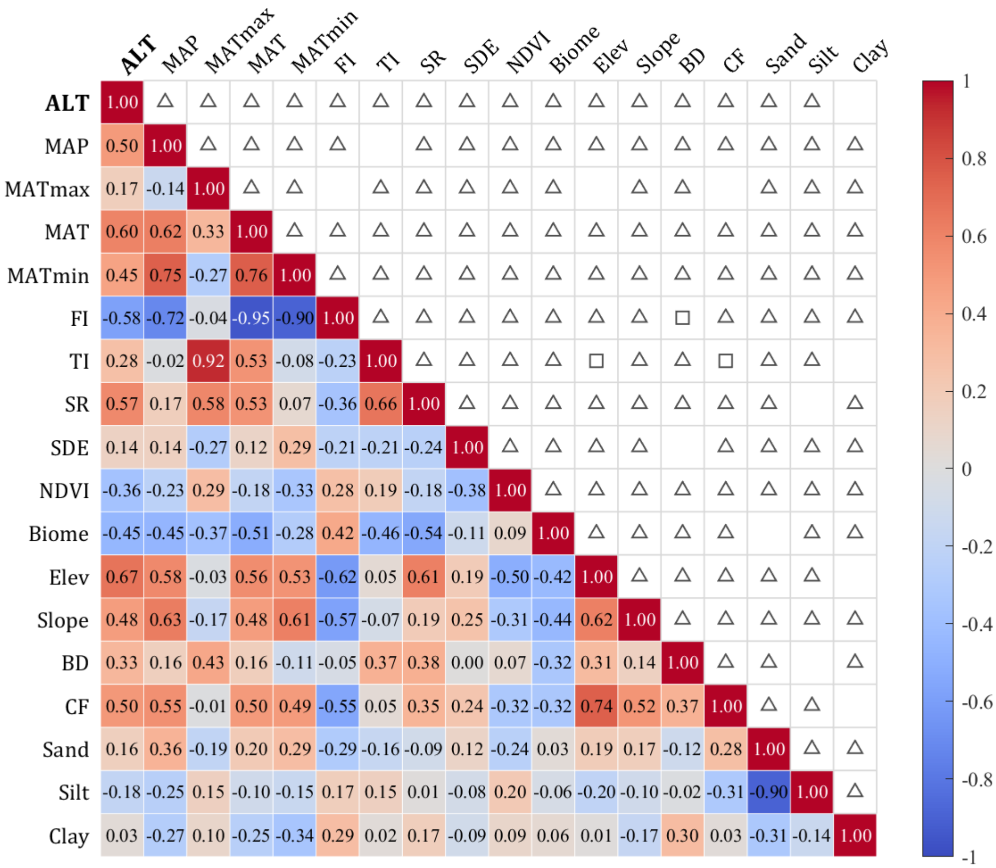

Figure 2. The correlation matrix between ALT and environmental covariates.

3.2 Model performance evaluation

3.2.1 Spatial prediction performance

The predictive performance of the five machine-learning models was evaluated using LOSO-CV (Table 1). Overall, all models showed comparable predictive skill, with R^2 values ranging from 0.693 to 0.752, RMSE values from 61.54 to 68.54 cm, MAE values from 32.13 to 35.43 cm, and CCC values between 0.839 and 0.865. Among the individual models, LightGBM achieved the highest predictive accuracy (R^2 = 0.752, r = 0.869, RMSE = 61.54 cm, MAE = 32.13 cm, CCC = 0.865), followed closely by CatBoost (R^2 = 0.747, r = 0.865, RMSE = 62.18 cm, MAE = 32.55 cm, CCC = 0.860). In comparison, XGBoost showed relatively lower performance, whereas RF and GBDT produced intermediate results.

The observed-versus-predicted distributions further illustrate the behaviour of the individual models under LOSO-CV (Fig. S1). All models reproduced the overall increase in predicted ALT with increasing observed ALT, although deviations from the 1:1 line became more pronounced at larger ALT values. In particular, very large observed ALT values tended to be underestimated, indicating greater difficulty in transferring model relationships to sites with extreme thaw depths. The overall scatter patterns also varied with latitude, reflecting differences in the environmental conditions represented by the monitoring network.

Among the five individual models, CatBoost and LightGBM consistently achieved the best overall performance across the evaluation metrics and were therefore combined using a simple averaging ensemble strategy. The ensemble model achieved the highest overall performance, with an R^2 of 0.761, r of 0.873, RMSE of 60.48 cm, MAE of 31.43 cm, and CCC of 0.868 (Table 1). The ensemble predictions also showed a slightly tighter distribution around the 1:1 line than most individual models (Fig. S1). Therefore, the ensemble model was adopted to generate the final annual ALT dataset for the Northern Hemisphere.

Site-level mean bias further revealed substantial spatial variability in LOSO-CV performance across the monitoring network (Fig. S2). Most monitoring sites exhibited relatively small positive or negative biases, whereas larger deviations occurred at a limited number of locations. Both overestimation and underestimation were observed across different geographic regions, indicating that prediction errors were primarily site dependent rather than characterized by a consistent hemispheric-scale spatial pattern. These site-level results complement the overall validation statistics by illustrating the magnitude and spatial heterogeneity of prediction errors at locations completely excluded from model training.

Table 1. Spatial predictive performance of the five machine-learning models and the ensemble model based on leave-one-site-out cross-validation.

Model	R^2	r	RMSE (cm)	MAE (cm)	CCC
RF	0.738	0.864	63.269	32.833	0.862
GBDT	0.740	0.862	63.065	32.958	0.857
XGBoost	0.693	0.841	68.544	35.430	0.839
CatBoost	0.747	0.865	62.182	32.552	0.860
LightGBM	0.752	0.869	61.541	32.133	0.865
Ensemble model	0.761	0.873	60.480	31.430	0.868

3.2.2 Temporal prediction performance

The temporal performance of the model was evaluated using site-level out-of-fold predictions generated by LOSO-CV (Fig. 3). The observed and predicted Sen's slopes were significantly correlated (r = 0.73, p < 0.001), indicating that the model captured the spatial variability in long-term ALT change rates. Furthermore, 86.8% of the monitoring sites exhibited consistent trend directions between observations and predictions, and the mean absolute slope error was 0.602 cm yr^{-1}. These results indicate that the model can reproduce the general pattern and direction of long-term ALT change when applied to locations excluded from model training.

https://doi.org/10.5194/essd-2026-447
Preprint. Discussion started: 12 August 2026

The reproduction of interannual variability was further evaluated using the fluctuation amplitude ratio (FAR) derived from LOSO-CV predictions (Fig. 3b). The median FAR was 0.628, indicating that the model generally underestimated the magnitude of year-to-year ALT fluctuations. This behaviour reflects the difficulty of reproducing site-specific temporal variability using kilometre-scale environmental predictors. Local processes, including microtopographic variability, snow redistribution, soil moisture dynamics, vegetation heterogeneity, and measurement uncertainty, are not fully represented by the gridded predictors. Consequently, short-term fluctuations at individual monitoring sites tend to be smoothed, whereas long-term temporal changes are reproduced more reliably.

Time-series comparisons at six representative long-term monitoring sites further illustrate the differences between spatially withheld predictions and the final released product (Fig. S3). The selected sites span a range of Arctic coastal, continental, alpine, and transitional permafrost environments. LOSO-CV predictions showed varying degrees of site-specific deviation, including both overestimation and underestimation at different sites and periods, whereas predictions from the final model generally showed closer agreement with the observations after incorporating the complete monitoring dataset. Despite differences in absolute ALT magnitude at some sites, the comparisons illustrate that the final dataset generally follows the observed temporal evolution, while the LOSO-CV series provides a more conservative indication of model transferability to locations without local observations.

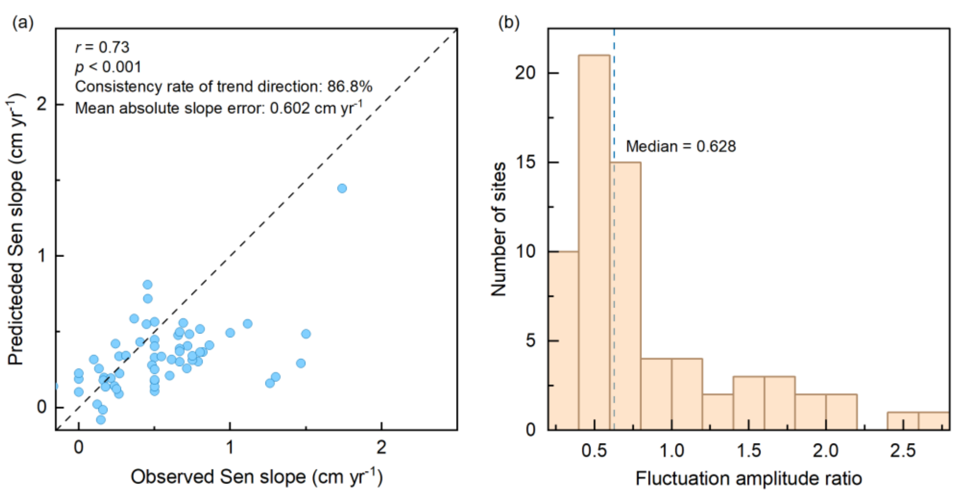

Figure 3. Temporal performance of the reconstructed ALT dataset based on leave-one-site-out cross-validation. (a) Comparison of observed and predicted Sen's slopes across the 68 monitoring sites with at least 10 years of observations during 2000–2020. The dashed line represents the 1:1 relationship. (b) Distribution of the fluctuation amplitude ratio (FAR) across the monitoring sites.

https://doi.org/10.5194/essd-2026-447
Preprint. Discussion started: 12 August 2026

3.3 Spatiotemporal pattern of ALT

Based on the optimal ensemble model, we reconstructed annual ALT across the Northern Hemisphere permafrost region from 2000 to 2024 (Fig. 4). ALT exhibited pronounced spatial heterogeneity, with a general pattern of shallow values at high latitudes and deeper values toward lower-latitude and marginal permafrost regions. ALT was generally below 100 cm in northern Siberia, the Canadian Arctic Archipelago, and northern Alaska, increased to approximately 100–150 cm across central Siberia and northern Canada, and exceeded 250 cm in some warmer or high-elevation marginal regions, including the Mongolian Plateau, Transbaikal, and parts of the Tibetan Plateau.

The hemispheric mean ALT increased from 120.62 cm in 2000 to 135.11 cm in 2024, corresponding to a cumulative increase of 14.49 cm (Fig. 4a–f). The increase was temporally uneven: mean ALT rose by 5.23 cm during 2000–2005, changed relatively little between 2005 and 2020, and then increased by 6.39 cm during 2020–2024. This pattern indicates an overall thickening of the active layer, accompanied by substantial interperiod variability.

The area proportions of different ALT classes also shifted toward deeper active layers (Fig. 4g). The proportions of areas with ALT <60 cm and 60–90 cm decreased from 15% and 36% in 2000 to 10% and 30% in 2024, respectively. In contrast, the proportions of the 90–120 cm, 120–150 cm, and >300 cm classes increased from 20%, 9%, and 6% to 23%, 13%, and 9%, respectively. The remaining intermediate classes changed only slightly. These changes collectively indicate a broad contraction of shallow active-layer areas and an expansion of moderate-to-deep active layers across the Northern Hemisphere permafrost region.

https://doi.org/10.5194/essd-2026-447
Preprint. Discussion started: 12 August 2026

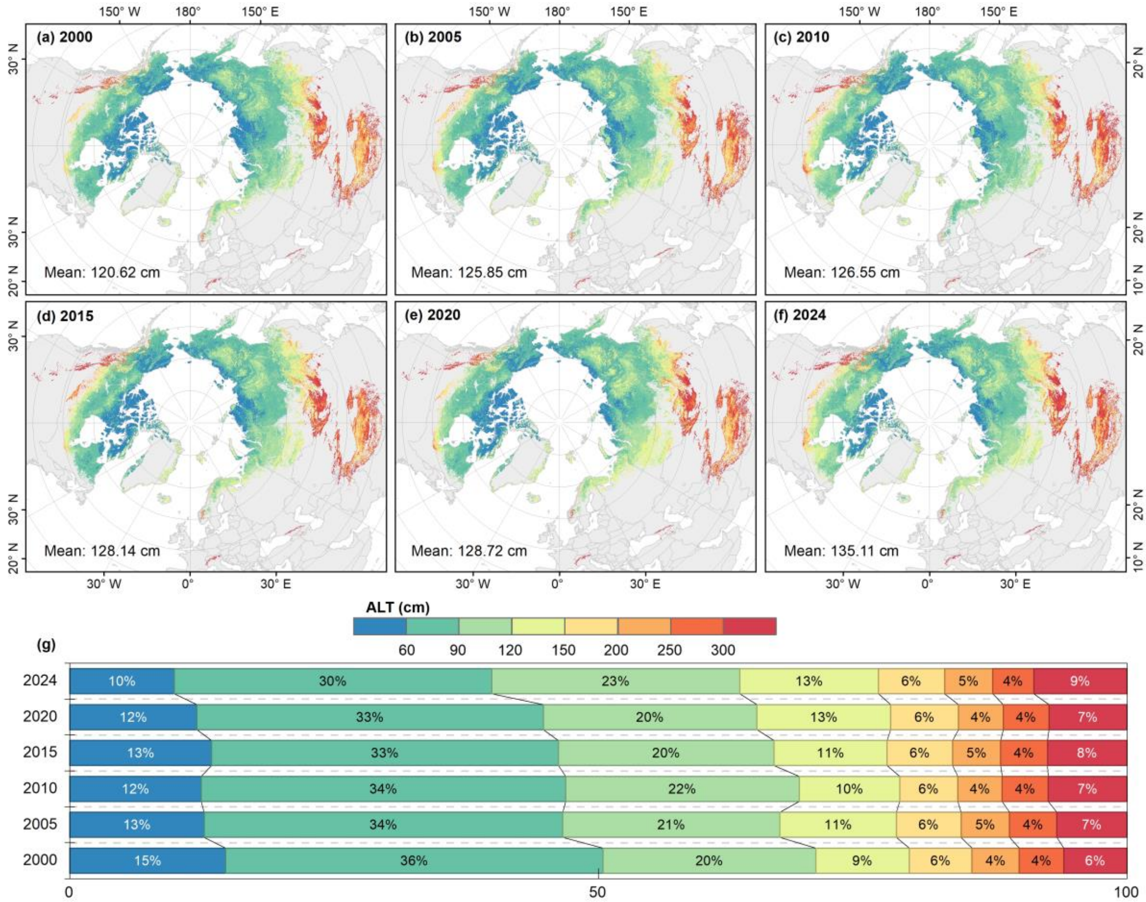

Figure 4. Spatiotemporal distribution of ALT (a–f) and the proportion of ALT area at different levels (g) from 2000 to 2024.

3.4 Geographic and ecological patterns of ALT

We examined ALT distributions along broad latitudinal and altitudinal gradients to characterize the large-scale geographic variations represented in the reconstructed dataset (Fig. 5). ALT showed a strongly nonlinear latitudinal pattern (Fig. 5a). Median ALT was generally high between 25 and 50°N, reaching its maximum in the 40–45°N band, whereas relatively lower values occurred at 30–40°N. North of 50°N, ALT declined markedly with increasing latitude, from approximately 130 cm at 50–55°N to around 60–100 cm at 70–85°N. This pattern reflects the combined effects of latitude and elevation, with the Tibetan Plateau moderating ALT at lower latitudes and deeper active layers occurring in lower-elevation marginal permafrost regions of Mongolia and southern Siberia.

The altitudinal relationship differed between Arctic and high-mountain permafrost regions. North of 60°N, median ALT remained relatively stable below 1.0 km elevation but increased markedly above 1.2 km, reaching approximately 140–150 cm at 1.4–2.0 km (Fig. 5b). This pattern likely reflects differences in surface and subsurface conditions, because low-elevation Arctic landscapes are often characterized by wetlands, peatlands, thick organic layers, and poor drainage (Rouse, 2000),

https://doi.org/10.5194/essd-2026-447
Preprint. Discussion started: 12 August 2026

whereas higher elevations generally have better drainage and a greater proportion of mineral soils or exposed bedrock (Pan et al., 2016; Si et al., 2024). In contrast, ALT decreased consistently with elevation in high-altitude regions above 3.5 km (Fig. 5c). Median ALT declined from approximately 340 cm at 3.5–3.75 km to about 190–200 cm at 5.75–6.0 km, consistent with the effect of decreasing temperature on seasonal thaw depth (Karki et al., 2020). The reconstructed dataset reproduced the expected large-scale latitudinal zonation and contrasting altitudinal relationships across Arctic and high-mountain permafrost environments, supporting its broad physical plausibility.

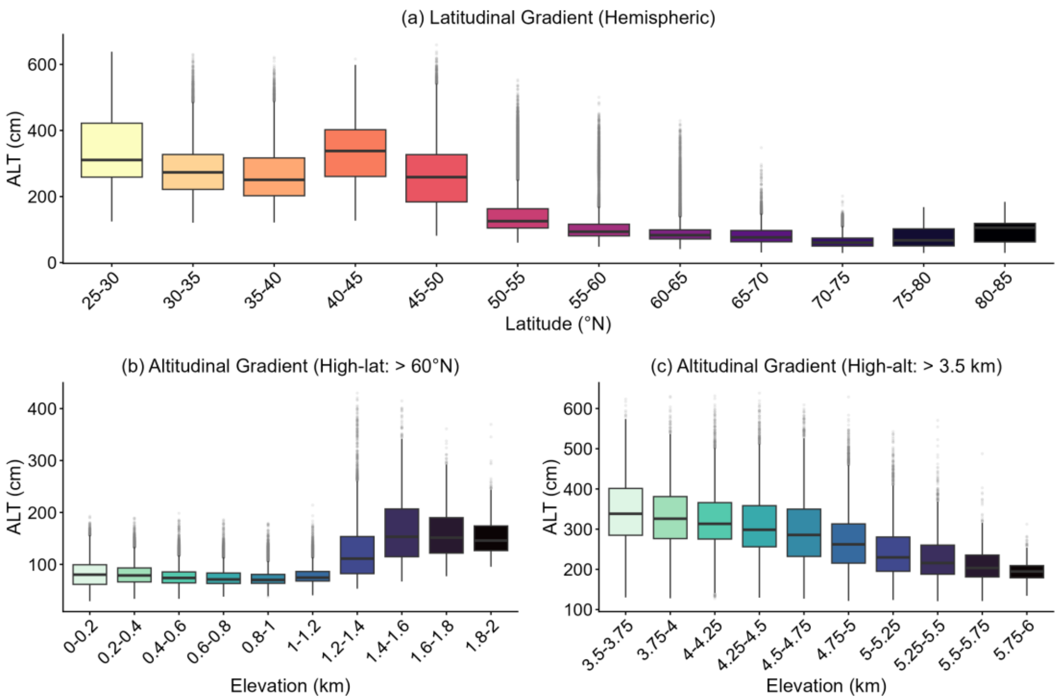

Figure 5. Macro-scale topographic and latitudinal patterns of ALT. (a) Hemispheric ALT distribution along the latitudinal gradient (binned at 5° intervals). (b) ALT variation along the altitudinal gradient in high-latitude Arctic regions (north of 60°N). (c) ALT variation along the altitudinal gradient in high-altitude, mid-to-low latitude regions (elevation > 3.5 km, typified by the Tibetan Plateau).

We further examined ALT distributions across different permafrost zones and biome types (Fig. 6). ALT increased progressively as permafrost continuity decreased (Fig. 6a). The mean ALT was lowest in continuous permafrost regions (110.14 cm), followed by discontinuous (136.27 cm), sporadic (143.66 cm), and isolated-patch permafrost regions (148.28 cm). This monotonic gradient is broadly consistent with the decline in permafrost thermal stability from continuous to isolated permafrost. However, the relatively small differences among discontinuous, sporadic, and isolated-patch zones indicate substantial overlap in ALT distributions, reflecting the strong spatial heterogeneity within each permafrost class.

https://doi.org/10.5194/essd-2026-447
Preprint. Discussion started: 12 August 2026

ALT also varied markedly among biome types (Fig. 6b). Tundra and boreal forest exhibited the shallowest mean ALT values, at 78.10 and 99.65 cm, respectively. Intermediate values occurred in temperate broadleaf and mixed forests (TeBMF, 166.56 cm) and flooded grasslands and savannas (FGS, 168.47 cm). In contrast, deserts and xeric shrublands (DXS) and montane grasslands and shrublands (MGS) showed the deepest mean ALT values, reaching 296.51 and 270.84 cm, respectively, followed by temperate coniferous forests (TeCF, 257.29 cm) and temperate grasslands, savannas, and shrublands (TeGSS, 226.80 cm). The broad distributions observed for several biome classes, particularly TeCF and TeGSS, indicate pronounced within-biome heterogeneity. Overall, the differences among permafrost zones and biome types were broadly consistent with known variations in regional climate, vegetation cover, soil properties, and surface energy exchange.

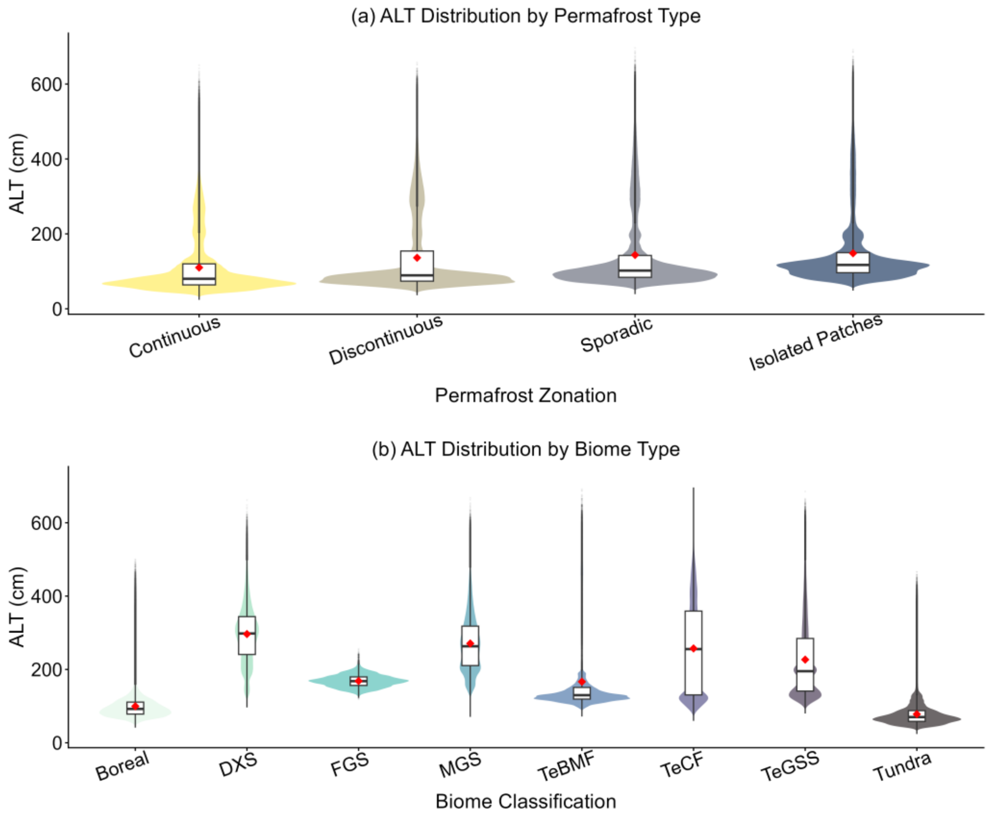

Figure 6. Statistical distribution of ALT across different permafrost zones and biome types. In each panel, the shaded violin shape represents the full probability density distribution of pixel-wise ALT predictions. Within the nested boxplots, the horizontal solid line indicates the median, the box boundaries represent the interquartile range (25th to 75th percentiles), and the red diamonds denote the arithmetic means. DXS, Deserts and Xeric Shrublands; FGS, Flooded Grasslands and Savannas; MGS, Montane Grasslands and Shrublands; TeBMF, Temperate Broadleaf and Mixed Forests; TeCF, Temperate Coniferous Forests; TeGSS, Temperate Grasslands, Savannas, and Shrublands.

https://doi.org/10.5194/essd-2026-447
Preprint. Discussion started: 12 August 2026

3.5 Comparison with other datasets

To contextualize the reconstructed dataset, we compared it with two recently published 1 km hemispheric ALT products: the physics-based product of Westermann et al. (2024) and the machine-learning product of Peng et al. (2024) (Figs. 7 and 8). The three datasets exhibited substantial differences in both magnitude and spatial structure, reflecting differences in model formulation, predictor information, and the representation of regional environmental heterogeneity.

The Westermann et al. (2024) product produced consistently shallower ALT estimates, with a Northern Hemisphere mean of 67.87 cm, compared with 125.71 cm in this study (Fig. 7a, b). This difference was evident across all representative regions, including Russia (72.43 vs. 97.43 cm), Mongolia (133.83 vs. 293.17 cm), the Tibetan Plateau (85.60 vs. 271.89 cm), Canada (52.79 vs. 93.13 cm), and Northern Europe (39.23 vs. 112.45 cm). The pixel-wise comparison further showed relatively weak spatial agreement between the two products, with Pearson's $r = 0.281$, an RMSE of 97.67 cm, and a mean difference of −46.70 cm, indicating that the Westermann product was generally shallower than our reconstruction (Fig. 8a).

In contrast, the Peng et al. (2024) product generated systematically deeper ALT estimates, with a hemispheric mean of 162.89 cm (Fig. 7c). The largest regional means occurred in Mongolia (330.50 cm), the Tibetan Plateau (284.87 cm), Canada (154.69 cm), and Russia (150.54 cm). Its spatial correspondence with our dataset was stronger than that of the physics-based product, with Pearson's $r = 0.622$, although substantial differences remained, as indicated by an RMSE of 93.17 cm and a positive mean difference of 58.41 cm (Fig. 8b). The pixel-wise comparison exhibited several distinct horizontal bands, indicating that many pixels in the Peng et al. (2024) product were assigned to similar ALT ranges.

Overall, our reconstruction occupied an intermediate position between the two existing products at the hemispheric scale, while displaying pronounced regional contrasts and visually finer spatial variability. This was particularly evident in Mongolia, the Tibetan Plateau, Alaska, and Canada, where our maps captured heterogeneous ALT patterns that were either strongly compressed in the physics-based product or more broadly generalized in the previous machine-learning product. These comparisons should not be interpreted as independent validation, but rather as evidence of the structural uncertainty that persists among current hemispheric ALT products.

https://doi.org/10.5194/essd-2026-447
Preprint. Discussion started: 12 August 2026

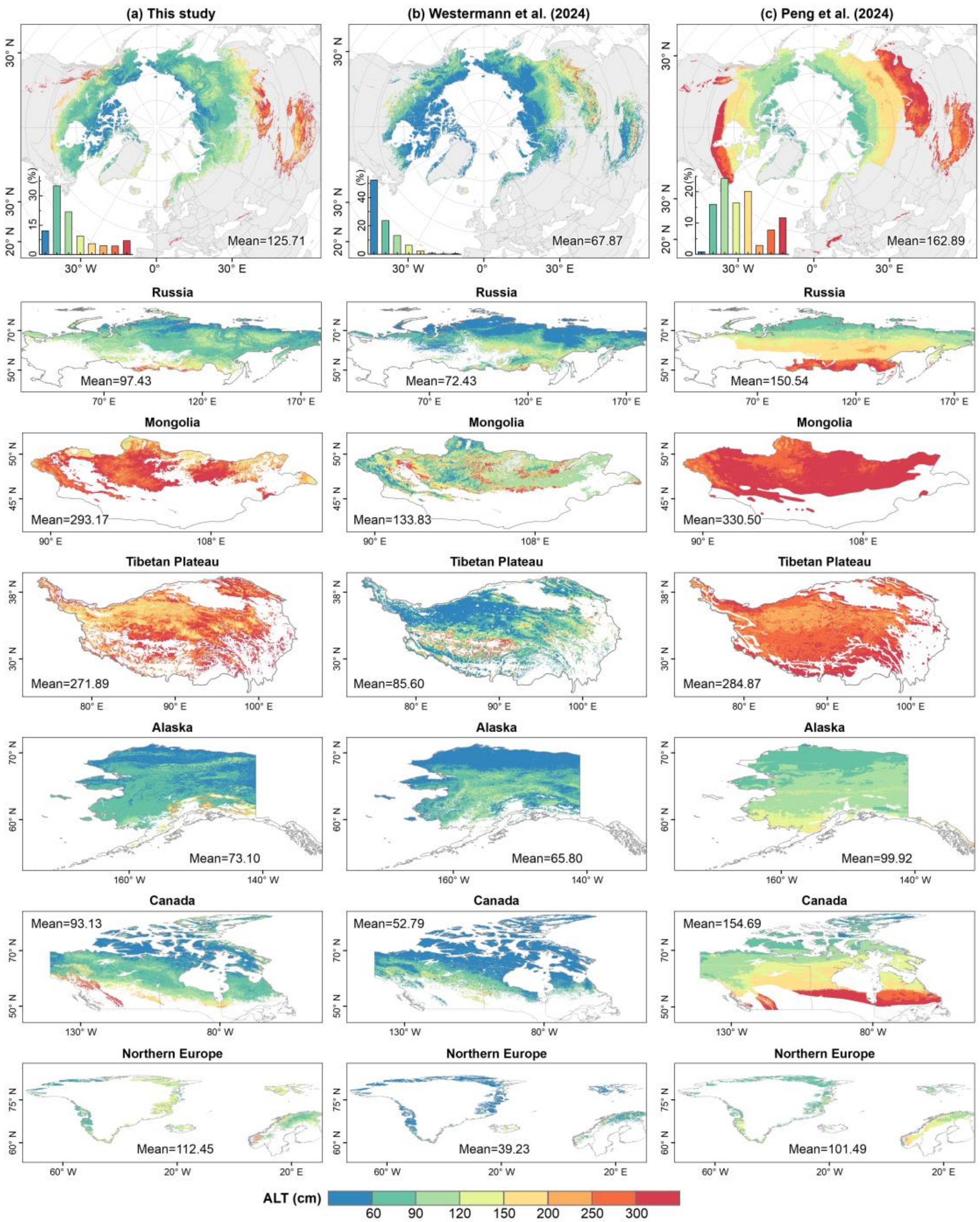

Figure 7. Spatial comparison of the reconstructed ALT dataset with existing 1 km hemispheric products. (a–c) Spatial distributions and regional mean ALT values for this study, Westermann et al. (2024), and Peng et al. (2024), respectively. The top row displays the overall hemispheric ALT distributions, with inset bar charts illustrating the frequency distributions (in percentages) of valid permafrost pixels and the exact domain-averaged mean values. The subsequent rows present localized

https://doi.org/10.5194/essd-2026-447
Preprint. Discussion started: 12 August 2026

spatial zoom-ins across six representative geographical units (Russia, Mongolia, the Tibetan Plateau, Alaska, Canada, and Northern Europe).

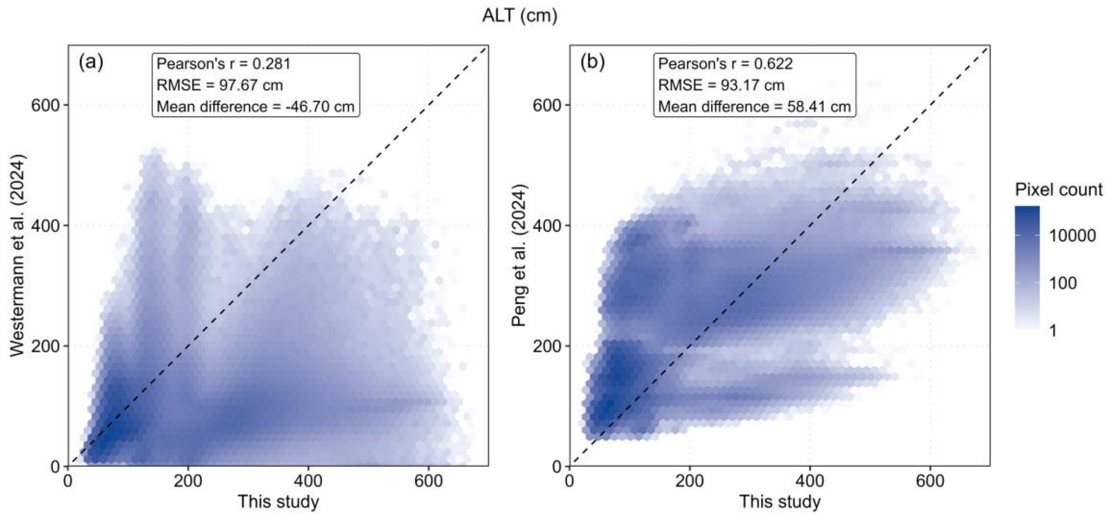

Figure 8. Pixel-wise comparison of mean ALT during 2000–2020 between this study and two existing hemispheric products. (a) Westermann et al. (2024) and (b) Peng et al. (2024), each compared with this study using 5 million randomly sampled common valid pixels. Dashed lines indicate the 1:1 relationship. RMSE and mean difference represent inter-product disagreement, with mean difference calculated as the existing product minus this study.

3.6 The uncertainty in ALT prediction

The predictive uncertainty showed a stable magnitude and spatial pattern across the Northern Hemisphere permafrost region during 2000–2024 (Fig. 9). Mean relative uncertainty varied only slightly, from 44.15% to 45.20% (Fig. 9a–f), while the proportional distribution among uncertainty classes remained broadly consistent. Approximately two-thirds of the permafrost area had uncertainty between 20% and 50%, whereas only 7%–8% exceeded 70% uncertainty (Fig. 9g). Spatially, uncertainty exhibited a heterogeneous and spatially discontinuous pattern. The relatively low uncertainty prevailed across extensive areas of Alaska, northern Canada, and northern Siberia. Given that these regions feature extensive carbon-rich soils and play a disproportionate role in climate–carbon feedbacks, reliable ALT estimates here are particularly critical (Hugelius et al., 2014; Schuur et al., 2015). Higher uncertainty occurred as scattered and discontinuous patches across several geographically separated regions, including parts of the Canadian Arctic Archipelago, Greenland, northeastern Siberia, and the Tibetan Plateau. This likely reflects region-specific combinations of complex terrain, fragmented land surfaces, strong local environmental gradients, and limited observational constraints. In these areas, local variations in climate, vegetation, snow cover, soil properties, and ground ice may not be fully represented by kilometre-scale predictors. The mapped uncertainty pattern provides an explicit measure of spatial confidence and supports the application of this dataset in large-scale permafrost, carbon-cycle, and ecosystem studies (Mishra et al., 2021).

https://doi.org/10.5194/essd-2026-447
Preprint. Discussion started: 12 August 2026

Open Access Earth System Science Data Discussions

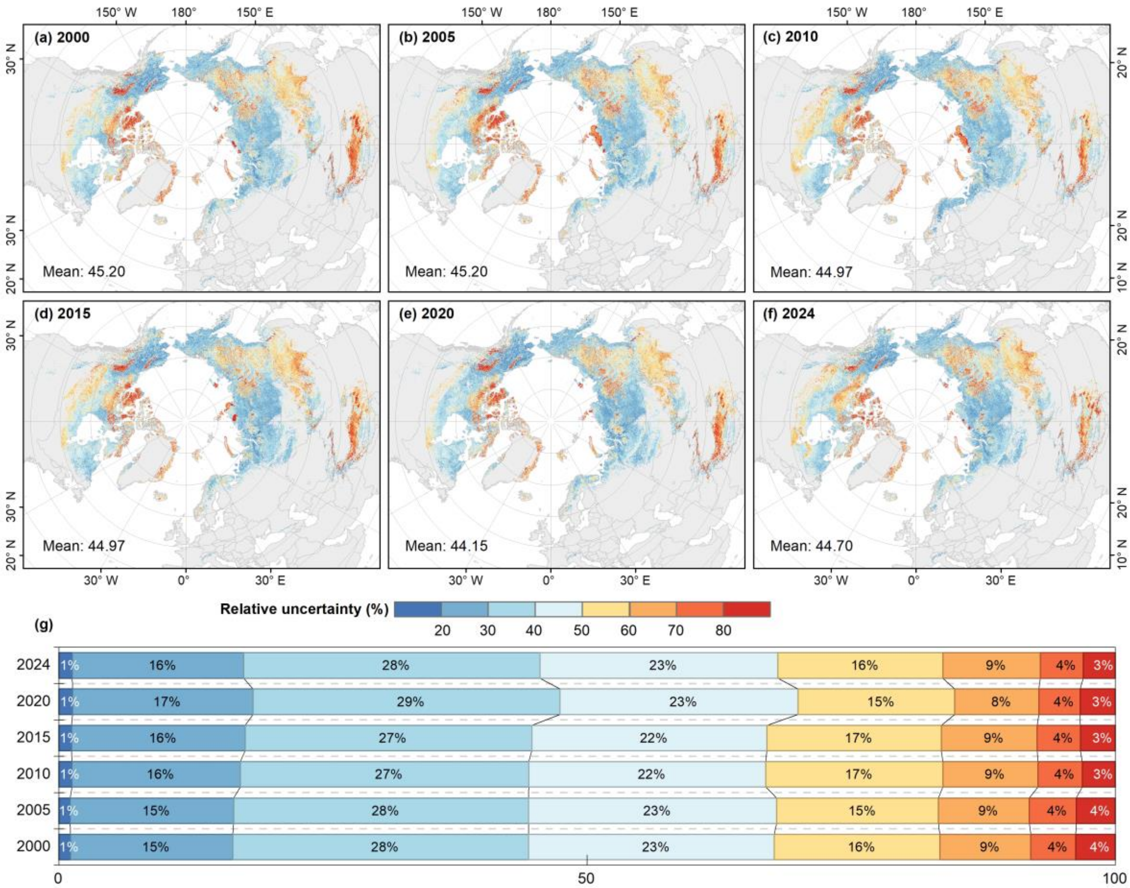

Figure 9. Spatiotemporal distribution of uncertainty in ALT prediction (a–f) and the proportions of areas at different uncertainty levels (g) from 2000 to 2024.

3.7 Potential applications and limitations

This study provides an annual, 1 km ALT dataset for the Northern Hemisphere permafrost region that can serve as a consistent baseline for investigating permafrost responses to climate change (Smith et al., 2022). The multi-model ensemble framework reduces dependence on any single algorithm and improves the robustness of predictions across diverse environmental conditions (Wang et al., 2020; Hu et al., 2024). Together with the spatially explicit uncertainty estimates and spatially independent LOSO-CV evaluation, the dataset is suitable for regional- to hemispheric-scale analyses of permafrost dynamics.

The dataset has potential applications in carbon-cycle, ecosystem, hydrological, and infrastructure studies. When combined with soil carbon and climate data, annual thaw-depth changes can help assess the exposure of previously frozen carbon and support the evaluation of permafrost–carbon feedbacks (Schuur et al., 2015; Harris et al., 2023; Lathrop et al., 2025; Mishra et al., 2021; Mu et al., 2016). The dataset can also be used to investigate changes in root-zone conditions, soil moisture, vegetation productivity, and surface hydrology. In addition, it provides baseline information for identifying broad

https://doi.org/10.5194/essd-2026-447
Preprint. Discussion started: 12 August 2026

areas where increasing thaw depth may elevate risks to roads, railways, pipelines, and settlements (Gartler et al., 2025; Jin et al., 2024b; Yang et al., 2010; Hjort et al., 2018).

Several limitations should be considered when using the dataset. Field observations remain spatially uneven, particularly in interior Siberia, the Canadian Arctic, and the Tibetan Plateau, making predictions in these regions more dependent on spatial extrapolation. LOSO-CV further showed that prediction errors varied among monitoring sites and that very large ALT values tended to be underestimated, indicating greater uncertainty under sparsely represented or extreme conditions. Such uncertainty is also a broader challenge in hemispheric-scale ALT mapping because thaw depth is strongly influenced by heterogeneous local conditions that are difficult to characterize consistently at large spatial scales, as reflected by the substantial differences among currently available ALT products (Peng et al., 2024; Westermann et al., 2024). In addition, most observations were collected during 2000–2020, so the 2021–2024 estimates should be regarded as model-based temporal extensions and interpreted with additional caution, particularly given the limited extrapolation capability of tree-based models. In addition, the fixed permafrost mask does not represent temporal changes in permafrost extent, and the 1 km resolution cannot fully capture local controls such as microtopography, ground ice, soil stratigraphy, snow redistribution, and fine-scale hydrological variability. Accordingly, the dataset is most appropriate for regional- to hemispheric-scale analyses rather than site-specific or short-term applications.

A further limitation concerns the interpretation of ALT in strongly degraded permafrost. Where incomplete winter refreezing leads to talik formation, the reported maximum thaw depth may represent the depth to the permafrost table rather than the thickness of a fully refreezing active layer (Farquharson et al., 2022; Romanovsky et al., 2010). For consistency with existing large-scale products, this study retains the term "ALT" as a practical descriptor of maximum annual thaw depth (Aalto et al., 2018; Peng et al., 2018, 2023; Ran et al., 2022). Accordingly, values in talik-affected regions should be interpreted as indicators of overall near-surface permafrost degradation rather than strictly classical active-layer thickness.

4 Data and code availability

The ALT dataset generated in this study is available online at https://doi.org/10.5281/zenodo.21667583 (Wei and Chen, 2026). The permafrost distribution data used in this study can be downloaded at PANGAEA (https://doi.org/10.1594/PANGAEA.888600). The ALT observations are available at the Circumpolar Active Layer Monitoring (CALM) program (https://www2.gwu.edu/~calm/data/north.htm). The monthly temperature and precipitation data were obtained from the WorldClim historical monthly weather dataset and are available at https://www.worldclim.org/data/worldclim21.html. Solar radiation and snow depth data can be obtained from ERA5-Land reanalysis data (https://cds.climate.copernicus.eu/datasets). The NDVI dataset from the Global 1km Resolution 2000-2024 Annual Maximum Composite Normalized Difference Vegetation Index (NDVI) Dataset can be downloaded at https://doi.org/10.57760/sciencedb.33612. The soil data can be extracted from SoilGrids database (https://soilgrids.org/). The DEM data can be downloaded at https://www.gebco.net/data_and_products/gridded_bathymetry_data/. The biome data is

https://doi.org/10.5194/essd-2026-447
Preprint. Discussion started: 12 August 2026

available at https://www.worldwildlife.org/publications/terrestrial-ecoregions-of-the-world. The codes used to generate ALT dataset are available to the public at https://github.com/WYJJJ12/ALT_Generate.git and is permanently deposited in a Zenodo repository at https://zenodo.org/records/21835259 (Wei, 2026).

5 Conclusions

This study developed a continuous annual ALT dataset at 1 km resolution for the Northern Hemisphere permafrost region from 2000 to 2024 using an ensemble spatiotemporal machine-learning framework. The dataset captures the major spatial patterns and interannual variability of ALT across diverse climatic, topographic, and ecological conditions. Spatial leave-one-site-out cross-validation yielded an ensemble R^2 of 0.76 and an RMSE of 60.48 cm, while temporal evaluation and pixel-wise uncertainty estimates further supported its reliability. Comparisons with two existing hemispheric products showed that our reconstruction occupied an intermediate position in hemispheric mean ALT, while preserving pronounced regional contrasts and relatively fine spatial variability. The substantial inter-product differences in both magnitude and spatial structure further highlight the structural uncertainty that persists in large-scale ALT mapping. The reconstructed time series also indicates a general deepening of ALT, demonstrating the dataset's capacity to characterize long-term permafrost change. Overall, the dataset provides a spatially detailed, temporally continuous, and uncertainty-explicit resource for regional- to hemispheric-scale permafrost studies. Estimates for recent years, data-sparse regions, and talik-affected areas should nevertheless be interpreted with appropriate caution.

Author contributions

YW and YC conceived the research. YW collected the data, wrote the manuscript, plotted the figures, and performed the analysis. YW and ZW interpreted the analytical results. YW, ZW, and JW contributed to the data validation. ZW, JW, HS and YC improved the writing and structure of the paper.

Competing interests

The contact author has declared that none of the authors has any competing interests.

Disclaimer

Publisher's note: Copernicus Publications remains neutral with regard to jurisdictional claims made in the text, published maps, institutional affiliations, or any other geographical representation in this paper. While Copernicus Publications makes every effort to include appropriate place names, the final responsibility lies with the authors.

https://doi.org/10.5194/essd-2026-447
Preprint. Discussion started: 12 August 2026

Acknowledgements

We gratefully acknowledge all data providers whose data have been used in this study.

Financial support

This work was supported by the Fundamental Research Funds for the Central Universities (grant no. 2042026kf0073).

References

Aalto, J., Karjalainen, O., Hjort, J., and Luoto, M.: Statistical forecasting of current and future Circum-Arctic ground temperatures and active layer thickness, Geophysical Research Letters, 45, 4889–4898, 2018.

Blois, J. L., Williams, J. W., Fitzpatrick, M. C., Jackson, S. T., and Ferrier, S.: Space can substitute for time in predicting climate-change effects on biodiversity, Proceedings of the National Academy of Sciences, 110, 9374–9379, 2013.

Chadburn, S. E., Burke, E. J., Cox, P. M., Friedlingstein, P., Hugelius, G., and Westermann, S.: An observation-based constraint on permafrost loss as a function of global warming, Nature Clim Change, 7, 340–344, 2017.

Cheng, G., Zhao, L., Li, R., Wu, X., Sheng, Y., Hu, G., Zou, D., Jin, H., Li, X., and Wu, Q.: Characteristic, changes and impacts of permafrost on Qinghai-Tibet Plateau, Chinese Science Bulletin, 64, 2783–2795, 2019.

Ding, K., Jiang, P., Ni, J., Shen, T., Yang, B., Zhang, R., and Yu, Z.: Machine learning uncovers a multi-year climate memory in permafrost degradation on the qinghai–tibet plateau: The critical roles of precipitation and lagged temperature, Journal of Hydrology, 663, 134272, 2025.

Farquharson, L. M., Romanovsky, V. E., Kholodov, A., and Nicolsky, D.: Sub-aerial talik formation observed across the discontinuous permafrost zone of alaska, Nat. Geosci., 15, 475–481, 2022.

Gartler, S., Scheer, J., Meyer, A., Abass, K., Bartsch, A., Doloisio, N., Falardeau, J., Hugelius, G., Irrgang, A., Haukur Ingimundarson, J., Jungsberg, L., Lantuit, H., Nymand Larsen, J., Lodi, R., Martin, V. S., Mercer, L., Nielsen, D., Overduin, P., Povoroznyuk, O., Rautio, A., Schweitzer, P., Speetjens, N. J., Tomaškovičová, S., Timlin, U., Vanderlinden, J.-P., Vonk, J., Westerveld, L., and Ingeman-Nielsen, T.: A transdisciplinary, comparative analysis reveals key risks from Arctic permafrost thaw, Commun Earth Environ, 6, 21, 2025.

Gasser, T., Kechiar, M., Ciais, P., Burke, E. J., Kleinen, T., Zhu, D., Huang, Y., Ekici, A., and Obersteiner, M.: Path-dependent reductions in CO2 emission budgets caused by permafrost carbon release, Nature Geosci, 11, 830–835, 2018.

Harris, L. I., Olefeldt, D., Pelletier, N., Blodau, C., Knorr, K.-H., Talbot, J., Heffernan, L., and Turetsky, M.: Permafrost thaw causes large carbon loss in boreal peatlands while changes to peat quality are limited, Global Change Biology, 29, 5720–5735, 2023.

Hjort, J., Karjalainen, O., Aalto, J., Westermann, S., Romanovsky, V. E., Nelson, F. E., Etzelmüller, B., and Luoto, M.: Degrading permafrost puts arctic infrastructure at risk by mid-century, Nat Commun, 9, 5147, 2018.

https://doi.org/10.5194/essd-2026-447
Preprint. Discussion started: 12 August 2026

Hu, G., Zhao, L., Wu, T., Wu, X., Park, H., Fedorov, A., Wei, Y., Li, R., Zhu, X., Sun, Z., Ni, J., and Zou, D.: Spatiotemporal variations and regional differences in air temperature in the permafrost regions in the northern hemisphere during 1980–2018, Science of The Total Environment, 791, 148358, 2021.

Hu, G., Zhao, L., Zou, D., Wu, X., Li, R., Zhu, X., Su, Y., Wu, T., Wu, Y., and Ni, J.: Large variability in permafrost degradation over the Northern Hemisphere, CATENA, 246, 108440, 2024.

Hugelius, G., Strauss, J., Zubrzycki, S., Harden, J. W., Schuur, E. a. G., Ping, C.-L., Schirrmeister, L., Grosse, G., Michaelson, G. J., Koven, C. D., O'Donnell, J. A., Elberling, B., Mishra, U., Camill, P., Yu, Z., Palmtag, J., and Kuhry, P.: Estimated stocks of circumpolar permafrost carbon with quantified uncertainty ranges and identified data gaps, Biogeosciences, 11, 6573–6593, 2014.

IPCC: Climate Change 2021: The Physical Science Basis. Contribution of Working Group I to the Sixth Assessment Report of the Intergovernmental Panel on Climate Change., Cambridge University Press, Cambridge, UK, 2021.

Jin, H., Peng, X., Frauenfeld, O. W., Huang, Y., Guo, L., Luo, J., Yin, G., Zhao, G., and Mu, C.: The infrastructure cost of permafrost degradation for the Northern Hemisphere, Global Environmental Change, 84, 102791, 2024.

Karki, R., Hasson, S. ul, Schickhoff, U., Scholten, T., Böhner, J., and Gerlitz, L.: Near surface air temperature lapse rates over complex terrain: A WRF based analysis of controlling factors and processes for the central himalayas, Clim Dyn, 54, 329–349, 2020.

Koven, C. D., Ringeval, B., Friedlingstein, P., Ciais, P., Cadule, P., Khvorostyanov, D., Krinner, G., and Tarnocai, C.: Permafrost carbon-climate feedbacks accelerate global warming, Proceedings of the National Academy of Sciences, 108, 14769–14774, 2011.

Lathrop, E., See, C., Walker, X., Falvo, G., Axler, Z., Ebert, C., Kadej, S., Kelley, A., Ledman, J., Opfergelt, S., Rodenhizer, H., and Schuur, E. A. G.: Permafrost thaw accelerates old soil carbon release, outpacing new plant inputs during a 13-year tundra warming experiment, Global Change Biology, 31, e70609, 2025.

Li, J., Lai, G., Meng, L., Zohner, C. M., Peñuelas, J., Veraverbeke, S., Hjort, J., Ciais, P., Chen, Y., Li, X., and Wu, C.: Amplified arctic–boreal fire regimes from permafrost thaw feedbacks, Nat. Geosci., 1–12, 2026.

Liu, Z., Kimball, J. S., Ballantyne, A., Watts, J. D., Natali, S. M., Rogers, B. M., Yi, Y., Klene, A. E., Moghaddam, M., Du, J., and Zona, D.: Widespread deepening of the active layer in northern permafrost regions from 2003 to 2020, Environ. Res. Lett., 19, 014020, 2023.

McGuire, A. D., Anderson, L. G., Christensen, T. R., Dallimore, S., Guo, L., Hayes, D. J., Heimann, M., Lorenson, T. D., Macdonald, R. W., and Roulet, N.: Sensitivity of the carbon cycle in the arctic to climate change, Ecological Monographs, 79, 523–555, 2009.

Mishra, U., Hugelius, G., Shelef, E., Yang, Y., Strauss, J., Lupachev, A., Harden, J. W., Jastrow, J. D., Ping, C.-L., Riley, W. J., Schuur, E. A. G., Matamala, R., Siewert, M., Nave, L. E., Koven, C. D., Fuchs, M., Palmtag, J., Kuhry, P., Treat, C. C., Zubrzycki, S., Hoffman, F. M., Elberling, B., Camill, P., Veremeeva, A., and Orr, A.: Spatial heterogeneity and environmental predictors of permafrost region soil organic carbon stocks, Sci. Adv., 7, eaaz5236, 2021.

Mu, C., Zhang, T., Zhang, X., Cao, B., and Peng, X.: Sensitivity of soil organic matter decomposition to temperature at different depths in permafrost regions on the northern Qinghai-Tibet Plateau, European Journal of Soil Science, 67, 773–781, 2016.

https://doi.org/10.5194/essd-2026-447
Preprint. Discussion started: 12 August 2026

Mu, C., Zhang, G., Xiao, C., Wei, Y., and Gerhard, K.: Interpretation of the IPCC Sixth Assessment Report: permafrost changes and their impacts, Journal of Glaciology and Geocryology, 45, 306–317, 2023.

Nelson, F. E., Anisimov, O. A., and Shiklomanov, N. I.: Subsidence risk from thawing permafrost, Nature, 410, 889–890, 2001.

Ni, J., Wu, T., Zhu, X., Hu, G., Zou, D., Wu, X., Li, R., Xie, C., Qiao, Y., Pang, Q., Hao, J., and Yang, C.: Simulation of the present and future projection of permafrost on the qinghai-tibet plateau with statistical and machine learning models, Journal of Geophysical Research: Atmospheres, 126, e2020JD033402, 2021.

Obu, J., Westermann, S., Kääb, A., and Bartsch, A.: Ground temperature map, 2000-2016, northern hemisphere permafrost [dataset], Alfred Wegener Institute, Helmholtz Centre for Polar and Marine Research, Bremerhaven, PANGAEA, https://doi.org/10.1594/PANGAEA.888600, 2018.

Obu, J., Westermann, S., Bartsch, A., Berdnikov, N., Christiansen, H. H., Dashtseren, A., Delaloye, R., Elberling, B., Etzelmüller, B., Kholodov, A., Khomutov, A., Kääb, A., Leibman, M. O., Lewkowicz, A. G., Panda, S. K., Romanovsky, V., Way, R. G., Westergaard-Nielsen, A., Wu, T., Yamkhin, J., and Zou, D.: Northern hemisphere permafrost map based on TTOP modelling for 2000–2016 at 1 km2 scale, Earth-Science Reviews, 193, 299–316, 2019.

Olson, D. M., Dinerstein, E., Wikramanayake, E. D., Burgess, N. D., Powell, G. V. N., Underwood, E. C., D'amico, J. A., Itoua, I., Strand, H. E., Morrison, J. C., Loucks, C. J., Allnutt, T. F., Ricketts, T. H., Kura, Y., Lamoreux, J. F., Wettengel, W. W., Hedao, P., and Kassem, K. R.: Terrestrial ecoregions of the world: A new map of life on earth, BioScience, 51, 933, 2001.

Pan, X., Li, Y., Yu, Q., Shi, X., Yang, D., and Roth, K.: Effects of stratified active layers on high-altitude permafrost warming: A case study on the qinghai–tibet plateau, The Cryosphere, 10, 1591–1603, 2016.

Peng, X., Zhang, T., Frauenfeld, O. W., Wang, K., Luo, D., Cao, B., Su, H., Jin, H., and Wu, Q.: Spatiotemporal changes in active layer thickness under contemporary and projected climate in the Northern Hemisphere, Journal of Climate, 31, 251–266, 2018.

Peng, X., Zhang, T., Frauenfeld, O. W., Mu, C., Wang, K., Wu, X., Guo, D., Luo, J., Hjort, J., Aalto, J., Karjalainen, O., and Luoto, M.: Active layer thickness and permafrost area projections for the 21st Century, Earth's Future, 11, e2023EF003573, 2023.

Peng, X., Jin, H., and Zhao, G.: Long-term series kilometer-level active layer thickness data set in Northern Hemisphere (1850-2100) [dataset], 2024.

Ran, Y., Li, X., Cheng, G., Che, J., Aalto, J., Karjalainen, O., Hjort, J., Luoto, M., Jin, H., Obu, J., Hori, M., Yu, Q., and Chang, X.: New high-resolution estimates of the permafrost thermal state and hydrothermal conditions over the Northern Hemisphere, Earth Syst. Sci. Data, 14, 865–884, 2022.

Romanovsky, V. E., Drozdov, D. S., Oberman, N. G., Malkova, G. V., Kholodov, A. L., Marchenko, S. S., Moskalenko, N. G., Sergeev, D. O., Ukraintseva, N. G., Abramov, A. A., Gilichinsky, D. A., and Vasiliev, A. A.: Thermal state of permafrost in russia, Permafrost and Periglacial Processes, 21, 136–155, 2010.

Rouse, W. R.: The energy and water balance of high-latitude wetlands: Controls and extrapolation, Global Change Biology, 6, 59–68, 2000.

https://doi.org/10.5194/essd-2026-447
Preprint. Discussion started: 12 August 2026

Schuur, E. a. G., McGuire, A. D., Schädel, C., Grosse, G., Harden, J. W., Hayes, D. J., Hugelius, G., Koven, C. D., Kuhry, P., Lawrence, D. M., Natali, S. M., Olefeldt, D., Romanovsky, V. E., Schaefer, K., Turetsky, M. R., Treat, C. C., and Vonk, J. E.: Climate change and the permafrost carbon feedback, Nature, 520, 171–179, 2015.

Shen, T., Jiang, P., Ju, Q., Yu, Z., Chen, X., Lin, H., and Zhang, Y.: Changes in permafrost spatial distribution and active layer thickness from 1980 to 2020 on the Tibet Plateau, Science of The Total Environment, 859, 160381, 2023.

Si, J., Zhang, S., Niu, Y., Zhang, Y., Fan, Q., and Chen, Y.: The surface deformation of permafrost and active layer thickness in the upper reaches of the black river basin, revealed by InSAR observations and independent component analysis, Science of The Total Environment, 951, 175667, 2024.

Smith, S. L., O'Neill, H. B., Isaksen, K., Noetzli, J., and Romanovsky, V. E.: The changing thermal state of permafrost, Nat Rev Earth Environ, 3, 10–23, 2022.

Tananaev, N. and Lotsari, E.: Defrosting northern catchments: Fluvial effects of permafrost degradation, Earth-Science Reviews, 228, 103996, 2022.

Vabalas, A., Gowen, E., Poliakoff, E., and Casson, A. J.: Machine learning algorithm validation with a limited sample size, PLOS ONE, 14, e0224365, 2019.

Wang, C., Song, L., Li, L., Wang, X., Song, R., Mu, X., and Jiang, T.: Global 1 km Resolution 2000–2024 Annual Maximum Composite Normalized Difference Vegetation Index (NDVI) Dataset (V3) [dataset], Science Data Bank, https://doi.org/https://doi.org/10.57760/sciencedb.33612, 2026.

Wang, T., Yang, D., Fang, B., Yang, W., Qin, Y., and Wang, Y.: Data-driven mapping of the spatial distribution and potential changes of frozen ground over the tibetan plateau, Science of The Total Environment, 649, 515–525, 2019.

Wang, T., Yang, D., Yang, Y., Piao, S., Li, X., Cheng, G., and Fu, B.: Permafrost thawing puts the frozen carbon at risk over the Tibetan Plateau, Sci. Adv., 6, eaaz3513, 2020.

Wei, Y. and Chen, Y.: A 1 km resolution dataset of Northern Hemisphere permafrost active layer thickness (2000–2024) [dataset], Zenodo, https://zenodo.org/records/21667583, 2026.

Wei, Y.: Code for reconstructing northern hemisphere active layer thickness at 1 km resolution (2000–2024) [code], Zenodo, https://zenodo.org/records/21835259, 2026.

Wei, Y., Chen, Y., Wang, J., Yu, P., Xu, L., Zhang, C., Shen, H., Liu, Y., and Zhang, G.: Mapping soil organic carbon in fragmented agricultural landscapes: The efficacy and interpretability of multi-category remote sensing variables, Journal of Integrative Agriculture, 24, 4395–4414, 2025.

Wei, Y., Chen, Y., Wang, J., Sun, Z., Wang, B., Zhang, C., Wu, C., Zhao, T., and Shen, H.: Enhancing farmland soil carbon mapping: Integrating radar backscatter model and machine learning, Soil and Tillage Research, 258, 107055, 2026.

Westermann, S., Barboux, C., Bartsch, A., Delaloye, R., Grosse, G., Heim, B., Hugelius, G., Irrgang, A., Kääb, A. M., Matthes, H., Nitze, I., Pellet, C., Seifert, F. M., Strozzi, T., Wegmüller, U., Wieczorek, M., and Wiesmann, A.: ESA permafrost climate change initiative (permafrost_cci): Permafrost active layer thickness for the northern hemisphere, v4.0 [dataset], NERC EDS Centre for Environmental Data Analysis, https://dx.doi.org/10.5285/d34330ce3f604e368c06d76de1987ce5, 2024.

Xu, X., Zhang, Z., and and Wu, Q.: Simulation of permafrost changes on the qinghai–tibet plateau, China, over the past three decades, International Journal of Digital Earth, 10, 522–538, 2017.

https://doi.org/10.5194/essd-2026-447
Preprint. Discussion started: 12 August 2026

Yang, M., Nelson, F. E., Shiklomanov, N. I., Guo, D., and Wan, G.: Permafrost degradation and its environmental effects on the Tibetan Plateau: A review of recent research, Earth-Science Reviews, 103, 31–44, 2010.